# Hyperbolic method for magnetic reconnection process in steady state magnetohydrodynamics

Hubert Baty, Hiroaki Nishikawa

## ▶ To cite this version:

Hubert Baty, Hiroaki Nishikawa. Hyperbolic method for magnetic reconnection process in steady state magnetohydrodynamics. Monthly Notices of the Royal Astronomical Society, 2016, 459 (1), pp.624-637. ⟨10.1093/mnras/stw654⟩. ⟨hal-03143027⟩

Monthly Notices
of the
ROYAL ASTRONOMICAL SOCIETY

MNRAS **459,** 624–637 (2016) doi:10.1093/mnras/stw654
Advance Access publication 2016 March 18

# Hyperbolic method for magnetic reconnection process in steady state magnetohydrodynamics

Hubert Baty[1]★ and Hiroaki Nishikawa[2]

[1] *Observatoire Astronomique de Strasbourg, Université de Strasbourg, CNRS UMR 7550, F-67000 Strasbourg, France*
[2] *National Institute of Aerospace, Hampton, VA 23666, USA*

Accepted 2016 March 15. Received 2016 March 15; in original form 2016 January 27

## ABSTRACT

A recent numerical approach for solving the advection-diffusion and Navier–Stokes equations is extended for the first time to a magnetohydrodynamic (MHD) model, aiming in particular consistent improvements over classical methods for investigating the magnetic reconnection process. In this study, we mainly focus on a two-dimensional incompressible set of resistive MHD equations written in flux-vorticity scalar variables. The originality of the method is based on hyperbolic reformulation of the dissipative terms, leading to the construction of an equivalent hyperbolic first-order (spatial derivatives) system. This enables the use of approximate Riemann solvers for handling dissipative and advective flux in the same way. A simple second-order finite-volume discretization on rectangular grids using an upwind flux is employed. The advantages of this method are illustrated by a comparison to two particular analytical steady state solutions of the inviscid magnetic reconnection mechanism, namely the magnetic annihilation and the reconnective diffusion problems. In particular, the numerical solution is obtained with the same order of accuracy for the solution and gradient for a wide range of magnetic Reynolds numbers, without any deterioration characteristic of more conventional schemes. The amelioration of the hyperbolic method and its extension to time-dependent MHD problems related to solar flares mechanisms is also discussed.

**Key words:** magnetic reconnection – MHD – methods: numerical – Sun: flares.

## 1 INTRODUCTION

Magnetic reconnection is a fundamental process in laboratory and space plasmas, which allows the conversion of magnetic energy into bulk flow and heating. The understanding of magnetic reconnection is a major goal of theoretical plasma physics in order to explain explosive events like disruptions in fusion laboratory experiments and flares in the solar corona. For such collisional plasmas, the magnetohydrodynamic (MHD) model is commonly adopted as an excellent framework (Priest & Forbes 2000).

The MHD approximation is a single fluid description of plasma dynamics, where the electromagnetic properties are taken into account via coupling terms obeying Maxwell's equations. Typically, electrical currents can be generated by via fluid motions producing Lorentz forces on the fluid. The plasma resistivity (inverse of the electrical conductivity) representing the magnetic field dissipation is very small in plasmas of interest, but it cannot be neglected as it precisely drives the reconnection process. It is thus crucial to treat with special care the resistivity term in numerical codes.

Most conventional MHD codes are based on shock-capturing methods using different Riemann-type solvers in order to handle discontinuities and shocks, as for example in the finite-volume based code AMRVAC (Porth et al. 2014). Such methods are particularly adapted and efficient for purely hyperbolic equations. This is however not the case of the resistive MHD model. In conventional MHD codes, the resistive term is generally computed by a separated scheme (using a finite-difference source term approximation for example), making the comparison between the evaluation of the advective flux and the resistive one not fully consistent. The reason for this separated treatment is due to different orders of spatial derivative of the main variable defining the fluxes, i.e. first and second order for the advective and dissipative flux, respectively (Gassner, Lorcher & Munz 2007). An example of inconsistent behaviour due to inconsistent construction of diffusive flux has been pointed out in the context of 2D advection-diffusion problem. Indeed, a strong degradation of the order of accuracy has been observed for Reynolds numbers of order unity, when compared to pure advective/diffusive limits (Nishikawa & Roe 2004; Nishikawa 2012). In MHD context, magnetic reconnection solutions involve large regions where the advection is dominant (i.e. where the local magnetic Reynolds number is much greater than one) and smaller regions where the diffusion is dominant (i.e. where the local magnetic Reynolds number

---

★ E-mail: hubert.baty@unistra.fr

Published by Oxford University Press on behalf of the Royal Astronomical Society

is much lower than one). A local deterioration of the spatial accuracy could propagate towards other regions and affect the solution in the whole domain. Moreover, as the existence of magnetic reconnection solutions is also very sensitive to the detailed spatial profile of the resistivity parameter (Baty, Forbes & Priest 2014), a careful treatment of the dissipation terms is clearly required. It has also been shown that classical high-resolution MHD codes lack convergence properties when addressing chaotic regimes of reconnection inherent of high Reynolds numbers plasmas (Keppens et al. 2013). Thus, as magnetic reconnection involves numerically challenging problems, it is clearly appealing for improved numerical schemes.

The hyperbolic approach initially introduced for the diffusion equation (Nishikawa 2007, 2014), and extended to advection-diffusion (Nishikawa 2010), or Navier–Stokes equations (Nishikawa 2011), could help to cure the above inconsistency. The basic idea is to transform the diffusive terms into hyperbolic ones by introducing diffusive fluxes as additional variables. These new variables that are gradients of the main variables, are also solutions of additional hyperbolic equations. Despite the common idea of using flux variables, this approach is different from the called mixed methods commonly employed in fluid mechanics (Younes, Ackerer & Chavent 2004). This method has several advantages over traditional approaches. First, as a fully hyperbolic system is obtained, the discretization scheme used for the non-dissipative part of the equations can be directly applicable to the dissipative terms. Secondly, the diffusive fluxes can be computed to the same order of accuracy as the main solution. Finally, a speed-up factor of $O(1/h)$ is generally obtained ($h$ being the typical mesh spacing).

The aim of the present study is to focus on the essential ideas. We construct a relatively simple second-order finite-volume method using an upwind approximate Riemann solver, even though other modern numerical methods like residual-distribution or discontinuous Galerkin discretization are also compatible with our problem. A simple rectangular grid is also considered for the spatial discretization. The plan of the paper is as follows. Section 2 presents the two-dimensional (2D) set of resistive/viscous MHD equations and also a simplified one-dimensional (1D) model equation. In Section 3, we introduce the principles of hyperbolization and associated numerical procedure to find stationary solutions of the model equation. Section 4 is devoted to the extension of the hyperbolic method to the MHD model. Even though we focus on inviscid resistive reconnection application in this work, the viscous term is also hyperbolized for the sake of generality. Numerical results for a 1D steady dissipative central layer problem are presented in Section 5. Section 6 presents the comparison of 2D stationary magnetic reconnection solutions obtained using our method with exact analytical inviscid solutions of two configurations. Finally, we discuss possible ameliorations of our scheme and extensions to more general problems, including time-dependent solutions for which non-uniform resistivity/viscosity coefficients play also an important role.

## 2 THE INCOMPRESSIBLE MHD MODEL

We consider the 2D incompressible set of dissipative (viscous and resistive) MHD equations written in flux-vorticity scalar variables as follows:

$$\frac{\partial \psi}{\partial t} + \boldsymbol{V}.\nabla\psi = \eta\nabla^2\psi + E(x, y), \qquad (1)$$

$$\frac{\partial \Omega}{\partial t} + \boldsymbol{V}.\nabla\Omega = \nu\nabla^2\Omega + \boldsymbol{B}.\nabla J, \qquad (2)$$

where the main variables are the magnetic flux function $\psi(x, y)$, and the scalar vorticity $\Omega(x, y)$. Both are functions of the 2D Cartesian space coordinates $(x, y)$. The magnetic field vector $\boldsymbol{B}$ is related to $\psi$ via $\boldsymbol{B} = (\frac{\partial\psi}{\partial y}, -\frac{\partial\psi}{\partial x})$. The fluid velocity $\boldsymbol{V} = (V_x, V_y)$ is related to $\Omega$ via $\nabla \times \boldsymbol{V} = \Omega\boldsymbol{k}$ with $\boldsymbol{k}$ is the unit vector perpendicular to the $(x, y)$ plane. The scalar variable $J$ is the current density (i.e. component of the current density perpendicular to the 2D plane) that can be deduced from the main variable trough $J = -\nabla^2\psi$ as a consequence of Ampere's law, taking the magnetic permeability constant equal to one in our units. The dissipative terms are the second derivatives terms involving the viscosity coefficient $\nu$ in $\Omega$-equation, and the resistivity coefficient $\eta$ in $\psi$-equation. For simplicity, these dissipative coefficients are assumed constant and uniform in this work, as steady state solutions are generally associated with spatially uniform resistivity. The source term $E$ represents a given electric field component perpendicular to the plane. Compared to a more conventional formulation using magnetic field and fluid velocity vectors as main variables, this set of equations has the advantage of ensuring the divergence free conditions on $\boldsymbol{B}$ and $\boldsymbol{V}$ (Orszag & Tang 1979).

Two extra equations must however be introduced in order to deduce the fluid velocity components from the two main variables, that can be shown to be (using the incompressibility assumption $\nabla.\boldsymbol{V} = 0$), namely

$$\nabla^2 V_x = -\frac{\partial\Omega}{\partial y}, \qquad (3)$$

$$\nabla^2 V_y = \frac{\partial\Omega}{\partial x}. \qquad (4)$$

### 2.1 A simplified 1D model equation

For the sake of introducing the basic concepts of the hyperbolic method and testing its essential properties, we also consider a simplified 1D equation that is a linear advection-diffusion equation for the main variable $\psi(x)$:

$$\frac{\partial\psi}{\partial t} + \frac{\partial(V\psi)}{\partial x} = \eta\frac{\partial^2\psi}{\partial x^2} + E(x), \qquad (5)$$

with $V(x)$ and $E(x)$ the given velocity and source term, respectively. The dissipative coefficient is $\eta$.

## 3 HYPERBOLIC METHOD FOR THE SIMPLIFIED 1D EQUATION

### 3.1 Hyperbolization: finding steady state solutions

Following previously related works on the hyperbolic method, we consider the following hyperbolic system (equivalent to the previous second-order derivative model equation 5):

$$\frac{\partial\psi}{\partial\tau} + \frac{\partial(V\psi)}{\partial x} - \frac{\partial(\eta p)}{\partial x} = E(x), \qquad (6)$$

$$\frac{\partial p}{\partial\tau} - \frac{1}{T_{\rm r}}\frac{\partial\psi}{\partial x} = -\frac{1}{T_{\rm r}}p, \qquad (7)$$

where $p$ is an additional variable, and $\tau$ is a pseudo-time. The crucial remark is that, solving these two equations in the pseudo-steady state (i.e. for vanishing pseudo-time derivative terms) is equivalent of solving the original equation in the true steady state, as $p$ is the $x$ derivative of $\psi$ in this limit. $T_{\rm r}$ is a relaxation time parameter defined as

$$T_{\rm r} = \frac{L_{\rm r}^2}{\eta}, \qquad (8)$$

where $L_{\mathrm{r}}$ is a length-scale parameter. The hyperbolic method is different from classical relaxation methods, which result in stiff relaxation systems because of the requirement of a vanishing equivalent relaxation time (Lowrie & Morel 2002). In our model, $T_{\mathrm{r}}$ is not required to vanish because our hyperbolic model reduces to the advection-diffusion equation exactly in the steady state for any non-zero $T_{\mathrm{r}}$. The choice of the $L_{\mathrm{r}}$ value, which also determines the $T_{\mathrm{r}}$ value, is mainly based on fast steady convergence requirement. For example, an optimal value of $L_{\mathrm{r}} = 1/(2\pi)$ has been proposed in diffusion problems (Nishikawa 2007). A different optimal formula for $L_{\mathrm{r}}$ has been derived for advection-diffusion problems with a uniform velocity (Nishikawa 2010), which shows that the optimal $L_{\mathrm{r}}$ value depends on the Reynolds number and needs to be reduced for advection dominated cases (i.e. for large Reynolds numbers). However, as one can see below in the paper, we select different values based on our own convergence studies on the typical problems addressed here.

Note also that the use of the pseudo-time variable $\tau$ is important in order to distinguish with the true time evolution, as discussed in the last section. Another important point is that the diffusion term in equation (6, third therm) appears now as a diffusive flux, thanks to the $p$ variable that is the gradient of the main variable $\psi$ in the steady state.

### 3.2 Steady state: discretization and implementation

We re-write our system as

$$\frac{\partial \boldsymbol{U}}{\partial \tau} + \frac{\partial \boldsymbol{F}}{\partial x} = \boldsymbol{S}, \tag{9}$$

where $\boldsymbol{U} = \begin{pmatrix} \psi \\ p \end{pmatrix}$, $\boldsymbol{F} = \begin{pmatrix} V\psi - \eta p \\ -\psi/T_{\mathrm{r}} \end{pmatrix}$, and $\boldsymbol{S} = \begin{pmatrix} E \\ -p/T_{\mathrm{r}} \end{pmatrix}$. The flux $\boldsymbol{F}$ can be splitted into two terms, an advective one $\boldsymbol{F}^{\mathrm{a}}$ and a dissipative one $\boldsymbol{F}^{\mathrm{d}}$, with $\boldsymbol{F}^{\mathrm{a}} = \begin{pmatrix} V\psi \\ 0 \end{pmatrix}$, and $\boldsymbol{F}^{\mathrm{d}} = \begin{pmatrix} -\eta p \\ -\psi/T_{\mathrm{r}} \end{pmatrix}$.

We consider a finite-volume method with a spatial discretization of the solution $\boldsymbol{U}$, where $\boldsymbol{U}_j$ is defined as the cell average of the solution of the $j$th spatial grid cell centred at $x_j$. We also consider a Riemann problem for the $j$th cell where the fluxes are evaluated at the two cell interfaces $x_{j-1/2}$ and $x_{j+1/2}$, respectively. The semi-discrete discretization of the system with our cell-centred scheme over the dual volume $I_j = [x_{j-1/2}, x_{j+1/2}]$ is thus

$$\frac{\partial \boldsymbol{U}_j}{\partial \tau} = -\frac{1}{h}[\boldsymbol{F}_{j+1/2} - \boldsymbol{F}_{j-1/2}] + \frac{1}{h}\int_{I_j} \boldsymbol{S}\mathrm{d}x, \tag{10}$$

where $h$ is the grid cell volume (not necessarily uniform).

Steady state solutions of the previous system can be obtained by using a pseudo-time explicit iteration

$$\boldsymbol{U}_j^{n+1} = \boldsymbol{U}_j^{n} - \Delta\tau \mathrm{Res}_j^{n}, \tag{11}$$

where $n$ is the iteration counter, $\Delta\tau$ is the pseudo-time step, and $-\mathrm{Res}_j^{n}$ is the residual right-hand side of equation (10) which is required to vanish (up to a pre-defined given accuracy) when a steady state solution is obtained.

### 3.3 Numerical flux and source term evaluation

The numerical flux is computed using the upwind formula:

$$\boldsymbol{F}_{j+1/2} = \frac{1}{2}(\boldsymbol{F}_{\mathrm{L}} + \boldsymbol{F}_{\mathrm{R}}) - \frac{1}{2}|\mathbf{A}|(\boldsymbol{U}_{\mathrm{R}} - \boldsymbol{U}_{\mathrm{L}}), \tag{12}$$

where the subscripts L and R stand for the left- and right-hand sides of the cell interface situated at $x_{j+1/2}$, respectively. The first term is computed from an average value of the two fluxes $\boldsymbol{F}_{\mathrm{L}} = \boldsymbol{F}(U_{\mathrm{L}})$ and $\boldsymbol{F}_{\mathrm{R}} = \boldsymbol{F}(U_{\mathrm{R}})$. $\mathbf{A}$ is the Jacobian matrix, $\mathbf{A} = \frac{\partial F}{\partial U}$.

The full flux can be separated into advective and dissipative parts, $\boldsymbol{F}^{\mathrm{a}}_{j+1/2}$ and $\boldsymbol{F}^{\mathrm{d}}_{j+1/2}$, respectively. In an excellent approximation, the full absolute Jacobian can be separated in two parts, $|\mathbf{A}| = |\mathbf{A}^{\mathrm{a}}| + |\mathbf{A}^{\mathrm{d}}|$. The advective Jacobian $|\mathbf{A}^{\mathrm{a}}|$ has a non-zero eigenvalue that is equal to the local velocity $V$, while the dissipative Jacobian $|\mathbf{A}^{\mathrm{d}}|$ has the following eigenvalues $\lambda = \pm\sqrt{\eta/T_{\mathrm{r}}}$. Note that this formulation leads to the upwind flux separately constructed for advective and diffusive terms, which is equivalent in one dimension to the sometimes called Rusanov or local Lax–Friedrichs flux, because $|\mathbf{A}^{\mathrm{a}}|$ is scalar and $|\mathbf{A}^{\mathrm{d}}|$ is a diagonal matrix with the eigenvalues of the same magnitude. There is an alternative way that consist in computing the eigenvalues of the full Jacobian in order to get an exactly unified scheme, but leading to more complicated implementation (especially for MHD equations).

We can therefore construct a numerical scheme by using advective/dissipative numerical fluxes based on upwind-type formulation, and taking the maximum wave speeds to evaluate the Jacobians,

$$\boldsymbol{F}^{\mathrm{a}}_{j+1/2} = \begin{pmatrix} \frac{1}{2}[(V\psi)_{\mathrm{L}} + (V\psi)_{\mathrm{R}}] - \frac{a_n}{2}[\psi_{\mathrm{R}} - \psi_{\mathrm{L}}] \\ 0 \end{pmatrix}, \tag{13}$$

$$\boldsymbol{F}^{\mathrm{d}}_{j+1/2} = \begin{pmatrix} \frac{1}{2}[(-\eta p)_{\mathrm{L}} + (-\eta p)_{\mathrm{R}}] - \frac{1}{2}\sqrt{\eta/T_{\mathrm{r}}}[\psi_{\mathrm{R}} - \psi_{\mathrm{L}}] \\ \frac{1}{2}[(-\psi/T_{\mathrm{r}})_{\mathrm{L}} + (-\psi/T_{\mathrm{r}})_{\mathrm{R}}] - \frac{1}{2}\sqrt{\eta/T_{\mathrm{r}}}[p_{\mathrm{R}} - p_{\mathrm{L}}] \end{pmatrix}, \tag{14}$$

where $a_n = |V|$. It has been previously shown that the effect of using such resistive flux formulation is to introduce two artificial waves travelling in opposite directions at the same speed, $\sqrt{\eta/T_{\mathrm{r}}}$. However, at large time compared to $T_{\mathrm{r}}$, the waves are rapidly damped out and the characteristic features of the diffusion are recovered (Nishikawa 2007).

Finally, the source term is computed using a simple point integration approximation,

$$\int_{I_j} \boldsymbol{S}\mathrm{d}x \approx \boldsymbol{S}_j h = \begin{pmatrix} hE_j \\ -hp_j/T_{\mathrm{r}} \end{pmatrix}, \tag{15}$$

that is shown to be sufficient to not degrade the accuracy of the method.

### 3.4 CFL criterion for pseudo-time stepping

One may note that, as we use an explicit pseudo-time iteration to march towards the steady state, the value of the increment in the pseudo-time variable $\tau$ is limited by a criterion,

$$\Delta\tau = \mathrm{CFL} \times \mathrm{Min}\left[\frac{h}{\sqrt{\eta/T_{\mathrm{r}}} + a_n}\right], \tag{16}$$

which can be rewritten as

$$\Delta\tau = \mathrm{CFL} \times \mathrm{Min}\left[\frac{h}{\frac{\eta}{L_{\mathrm{r}}} + a_n}\right], \tag{17}$$

where CFL is the Courant–Friedrichs–Lewy number less than or equal to one. In this CFL criterion, we have approximated the maximum wave speed by using the sum of the ‘dissipative’ wave speed and local absolute velocity. As an important remark, this CFL limitation shows that the hyperbolic method has an advantage in the limit of small $h$ over the conventional explicit scheme where the criterion is

$$\Delta t = \mathrm{CFL} \times \mathrm{Min}\left[\frac{h}{a_n}, \frac{h^2}{\eta}\right], \tag{18}$$

leading to a $O(1/h)$ acceleration factor in dissipative dominated problems and/or high-resolution cases.

### 3.5 Left/right interfaces extrapolation

We use a second-order accuracy method, where the nodal gradients are evaluated by a linear least-squares (LSQ) method. The left and right states are thus evaluated by a linear extrapolation from the cell centres. More explicitly we use

$$\psi_{\mathrm{L}} = \psi_j + \frac{1}{2}h\nabla\psi_j, \quad \psi_{\mathrm{R}} = \psi_k - \frac{1}{2}h\nabla\psi_k, \tag{19}$$

$$p_{\mathrm{L}} = p_j + \frac{1}{2}h\nabla p_j, \quad p_{\mathrm{R}} = p_k - \frac{1}{2}h\nabla p_k, \tag{20}$$

where $\nabla\psi_j$ is the gradient of $\psi$ computed by the LSQ method at node $j$, and similarly for $\nabla p_j$ (we have $k = j + 1$).

An economic variant of this proposed scheme was first introduced in Nishikawa (2014) and called 'Scheme-II'. The idea is to use the variable $p_j$ in the evaluation of $\nabla\psi_j$ (in equation 19), as we have $p$ is the spatial derivative of $\psi$ in the steady state. This is also a second-order scheme that has been previously shown to converge rapidly towards the steady state. This scheme is precisely employed for the tests presented in this work. Slope limiters are not required as the problems investigated in this work have smooth solutions without true singularities. However, in problems involving shock formation for example, some limited reconstructions could be easily added to the scheme.

## 4 HYPERBOLIC METHOD FOR THE 2D MHD EQUATIONS

We now focus on the flux-vorticity MHD equations introduced in Section 2. The hyperbolization of the $\psi$ equation has been described in the previous section, and can be reformulated for the 2D flux equation as

$$\frac{\partial\psi}{\partial\tau} + \frac{\partial(V_x\psi)}{\partial x} + \frac{\partial(V_y\psi)}{\partial y} - \frac{\partial(\eta p_\psi)}{\partial x} - \frac{\partial(\eta q_\psi)}{\partial y} = E_\psi(x, y), \tag{21}$$

$$\frac{\partial p_\psi}{\partial\tau} - \frac{1}{T_\psi}\frac{\partial\psi}{\partial x} = -\frac{1}{T_\psi}p_\psi, \tag{22}$$

$$\frac{\partial q_\psi}{\partial\tau} - \frac{1}{T_\psi}\frac{\partial\psi}{\partial y} = -\frac{1}{T_\psi}q_\psi, \tag{23}$$

where we use the notation $p_\psi$ and $q_\psi$ for the $x$ and $y$ derivatives of $\psi$, respectively, in the true steady state, and where $E_\psi$ is the source term. We also introduce an associated relaxation time parameter, $T_\psi = L_{\mathrm{r}}^2/\eta$. The equation for the vorticity function $\Omega$ can be also hyperbolized in the same way:

$$\frac{\partial\Omega}{\partial\tau} + \frac{\partial(V_x\Omega)}{\partial x} + \frac{\partial(V_y\Omega)}{\partial y} - \frac{\partial(\nu p_\Omega)}{\partial x} - \frac{\partial(\nu q_\Omega)}{\partial y} = E_\Omega(x, y), \tag{24}$$

$$\frac{\partial p_\Omega}{\partial\tau} - \frac{1}{T_\Omega}\frac{\partial\Omega}{\partial x} = -\frac{1}{T_\Omega}p_\Omega, \tag{25}$$

$$\frac{\partial q_\Omega}{\partial\tau} - \frac{1}{T_\Omega}\frac{\partial\Omega}{\partial y} = -\frac{1}{T_\Omega}q_\Omega, \tag{26}$$

where the two associated gradient variables are now $p_\Omega$ and $q_\Omega$. A second corresponding relaxation time is also introduced, $T_\Omega = L_{\mathrm{r}}^2/\nu$, as a second dissipative coefficient $\nu$ (viscosity) is present for viscous plasmas. The source term $E_\Omega$ contains a very specific term, namely $\boldsymbol{B}.\nabla J$, with $\boldsymbol{B} = (B_x, B_y) = (q_\psi, -p_\psi)$ and $J = -\nabla^2\psi = -(\frac{\partial p_\psi}{\partial x} + \frac{\partial q_\psi}{\partial y})$. In conventional schemes, the latter term is very tricky as it involves third-order spatial derivative in $\psi$. This is the reason why the flux-vorticity formulation is in general not adopted, except in fully periodic configurations where the use of spectral Fourier basis simplifies the problem (Orszag & Tang 1979). In our discretization, as $\boldsymbol{B}.\nabla J = \nabla.(J\boldsymbol{B})$, we evaluate this term using a central flux

$$\frac{1}{2}[(JB_n)_{\mathrm{L}} + (JB_n)_{\mathrm{R}}], \tag{27}$$

where $B_n = B_x n_x + B_y n_y$. We use the notation $\boldsymbol{n} = (n_x, n_y)$ for the unit vector across two states, L (left) and R (right), at each cell interface.

The velocity components $(V_x, V_y)$ are computed using the vorticity trough, $\nabla^2 V_x = -\frac{\partial\Omega}{\partial y}$, and $\nabla^2 V_y = \frac{\partial\Omega}{\partial x}$. These two Poisson equations can also be hyperbolized, as we can write

$$\frac{\partial V_x}{\partial\tau} - \frac{\partial p_x}{\partial x} - \frac{\partial q_x}{\partial y} = \frac{\partial\Omega}{\partial y}, \tag{28}$$

$$\frac{\partial p_x}{\partial\tau} - \frac{1}{T_{\mathrm{r}}}\frac{\partial V_x}{\partial x} = -\frac{1}{T_{\mathrm{r}}}p_x, \tag{29}$$

$$\frac{\partial q_x}{\partial\tau} - \frac{1}{T_{\mathrm{r}}}\frac{\partial V_x}{\partial y} = -\frac{1}{T_{\mathrm{r}}}q_x, \tag{30}$$

for $V_x$ variable. In a similar way, we have

$$\frac{\partial V_y}{\partial\tau} - \frac{\partial p_y}{\partial x} - \frac{\partial q_y}{\partial y} = -\frac{\partial\Omega}{\partial x}, \tag{31}$$

$$\frac{\partial p_y}{\partial\tau} - \frac{1}{T_{\mathrm{r}}}\frac{\partial V_y}{\partial x} = -\frac{1}{T_{\mathrm{r}}}p_y, \tag{32}$$

$$\frac{\partial q_y}{\partial\tau} - \frac{1}{T_{\mathrm{r}}}\frac{\partial V_y}{\partial y} = -\frac{1}{T_{\mathrm{r}}}q_y, \tag{33}$$

for $V_y$ variable. Indeed, the $(x, y)$ gradient variables $(p_x, q_x)$, and $(p_y, q_y)$, are the partial derivatives of $V_x$ and $V_y$ in the steady state, respectively. A third relaxation time $T_{\mathrm{r}}$ is defined as $L_{\mathrm{r}}^2/1$.

### 4.1 Discretization and implementation

The general form of our MHD system can be written as

$$\frac{\partial\boldsymbol{U}}{\partial\tau} + \frac{\partial\boldsymbol{F}}{\partial x} + \frac{\partial\boldsymbol{G}}{\partial y} = \boldsymbol{S}, \tag{34}$$

where $\boldsymbol{U}$ is a vector variable containing 12 scalar functions, namely the 4 main variables and the 8 associated gradient variables. $\boldsymbol{F}$ and $\boldsymbol{G}$ represent the $x$-directed and $y$-directed fluxes respectively, and $\boldsymbol{S}$ is the source vector. The scalar components of these vectors are detailed in Appendix A1.

Following the previous section, the discretization form reads

$$\begin{aligned}\frac{\partial\boldsymbol{U}_{i,j}}{\partial\tau} = &-\frac{1}{h_x}[\boldsymbol{F}_{i,j+1/2} - \boldsymbol{F}_{i,j-1/2}]\\ &-\frac{1}{h_y}[\boldsymbol{G}_{i+1/2,j} - \boldsymbol{G}_{i-1/2,j}] + \frac{1}{h_x h_y}\int_{I_{i,j}}\boldsymbol{S}\mathrm{d}x\mathrm{d}y,\end{aligned} \tag{35}$$

where $h_x = x_{i,j+1/2} - x_{i,j-1/2}$ and $h_y = x_{i+1/2,j} - x_{i-1/2,j}$ are the grid cell spacings in $x$ and $y$ directions, respectively (see fig. A1 in appendix). The interfaces numerical fluxes and the numerical evaluation of the source term are detailed in Appendix A2 and A3, respectively. The pseudo-time explicit iteration is

$$\boldsymbol{U}_{i,j}^{n+1} = \boldsymbol{U}_{i,j}^{n} - \Delta\tau\mathrm{Res}_{i,j}^{n}, \tag{36}$$

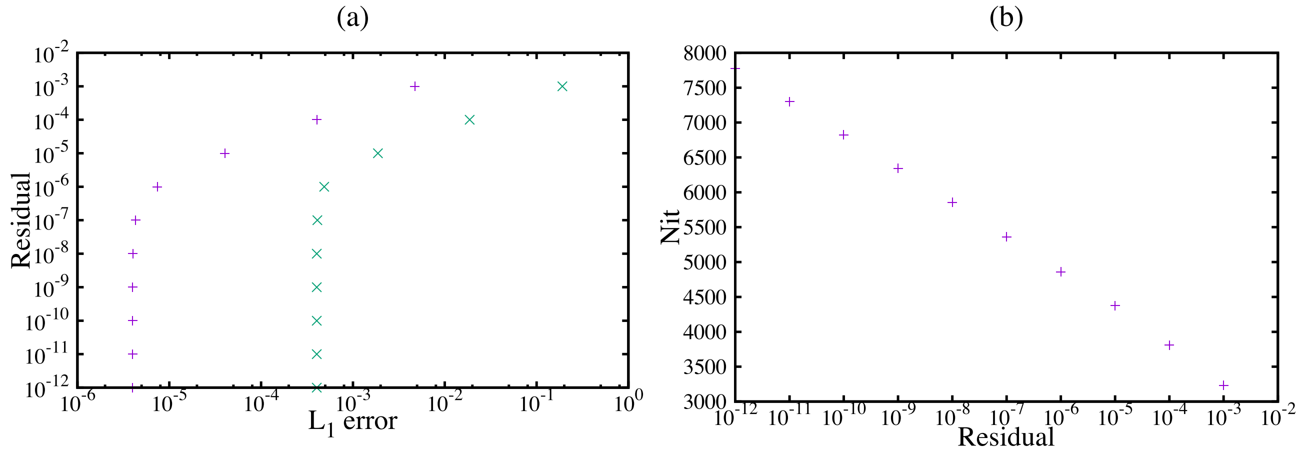

**Figure 1.** (a) Residual value (on $\psi$ and $p$) obtained as a function of the corresponding $L_1$ errors, illustrating the pseudo-time step convergence on the 1D central layer problem. (b) Corresponding number of iterations required as a function of the residual value. The number of grid cells is 4000 for this case $l = 0.01$, and $L_{\rm r}^{-1} = 20\pi$.

where $n$ is the iteration counter, $\Delta\tau$ is the pseudo-time step, and $-{\rm Res}_{i,j}^{n}$ is the residual right-hand side which should vanish (up to a pre-defined given accuracy) when the steady state is obtained. The pseudo-time step is limited by a CFL criterion (see Appendix A4).

## 5 STEADY DISSIPATIVE CENTRAL LAYER PROBLEM AS A TEST FOR THE 1D ADVECTION EQUATION

We consider the 1D advection-diffusion equation in $x \in [-L : L]$,

$$\frac{\partial \psi}{\partial t} + V(x)\frac{\partial \psi}{\partial x} - \eta \frac{\partial^2 \psi}{\partial x^2} = 0, \tag{37}$$

where a non-uniform velocity profile $V(x)$ is imposed with $V(x) = -V_0 \tanh(x/l)$, $l$ being given. We set $V_0 = 1$ and the domain length $L = 1$ to define our normalization. Thus, an exact stationary solution for $\psi$ follows the same dependence for the normalized dissipation parameter $\eta = l/2$, namely $\psi(x) = -\psi_0 \tanh(x/l)$ with $\psi_0 = 1$. Consequently, at high Reynolds number defined as $R_{\rm e} = LV_0/\eta$, this problem develops a narrow central layer around $x = 0$ with a characteristic thickness scaling as $l = 2\eta = 2/R_{\rm e}$. The central region exhibits a strong reversal in the main solution $\psi$ and a singular corresponding $p$ variation, which are more representative of a magnetic reconnection configuration than the wall boundary layer problem usually chosen to test numerical schemes.

As the velocity is not uniform, the hyperbolic method is used on the equation (equivalent form of equation 37)

$$\frac{\partial \psi}{\partial t} + \frac{\partial (V\psi)}{\partial x} - \eta \frac{\partial^2 \psi}{\partial x^2} = \psi \frac{\partial V}{\partial x}, \tag{38}$$

with an additional source term $E(x) = \psi \frac{\partial V}{\partial x}$ that is numerically evaluated using equation (15). The solution is thus computed inside the spatial domain $x \in [-1 : 1]$ with an exact Dirichlet boundary condition taken on the main variable $\psi$. Note that, such boundary condition is imposed in a weak form via the numerical flux at $x = \pm 1$ interfaces. The boundary gradient variable $p$ is simply computed using our numerical scheme. An initial guess dependence for $\psi(x)$ and gradient variable $p(x)$ must be provided in the domain interior, but the results are not very sensitive to it. Typically, we simply use $\psi(x) = p(x) = 0$ as initial values.

First, we examined the effect of the $L_{\rm r}$ parameter value on the convergence towards the steady solution. The steady state is considered to be obtained when the initial residual of the system (see equation 11) is reduced by nine orders of magnitude in the $L_1$ norm. The CFL number is taken to be 0.99 in all cases. The residual value is evaluated using the maximum residual component over the two variables, $\psi$ and $p$. Choosing a relative final value of $10^{-9}$ for the residual is shown to be largely sufficient for an acceptable stopping criterion in this problem, as can be seen in Fig. 1. Indeed, the method has already converged to the machine precision, and asking for a lower residual value would just result in larger computation time because of a higher number of required iterations (right-hand panel of Fig. 1). When $l = 1$ and 0.1, the optimal value obtained for the fastest convergence is close to the $L_{\rm r}^{-1} = 2\pi$ value deduced for a purely diffusion equation. However, the optimal value is progressively shifted towards lower $L_{\rm r}$ values as $l$ is reduced. This is illustrated in Fig. 2 for $l = 10^{-2}$ and $10^{-3}$. The optimal $L_{\rm r}$ is not exactly the same for the minimum $L_1$ error and for the minimum iteration number, but an average value of $L_{\rm r}^{-1} \approx 16\pi$ and $L_{\rm r}^{-1} \approx 256\pi$ can be deduced for cases $l = 10^{-2}$ and $10^{-3}$, respectively. An even lower optimal $L_{\rm r}$ with $L_{\rm r}^{-1} \approx 2048\pi$ is required for $l = 10^{-4}$. This result is not surprising as the system becomes progressively advecting dominated when $\eta = l/2$ is decreased (and $R_{\rm e}$ is increased). Secondly, we verified the expected spatial order of accuracy of the scheme for a wide range of the Reynolds number, $R_{\rm e} \in [2 : 2 \times 10^4]$. The $L_1$ error convergence results are shown in Figs 3 and 4 for five values of the $l$ parameter. The hyperbolic scheme clearly gives a second-order accuracy in the solution $\psi$ and gradient $p$ for a wide range of dissipation parameter values, as $\eta = l/2$ for this problem. This is true for a uniform grid (cases in Fig. 3), and also for the non-uniform grid used for the $l = 0.0001$ case (left-hand panel in Fig. 4). A zoom on the solution obtained for the latter case with 2000 cells is displayed in Fig. 5, which demonstrates the ability of the scheme to capture the singular central layer. In the non-uniform grid case, the grid is stretched in order to get 18 cells in the $x$-range $[-0.001 : 0.001]$ compared to three cells for a similar uniform grid.

Finally, the total number of iterations for convergence is plotted in right-hand panel of Fig. 4 for two cases. The other cases are not shown because they look very similar. A linear dependence with the number of grid cells is clearly observed, as expected form the CFL criterion on the pseudo-time step in $O(1/h)$ (see equation 16).

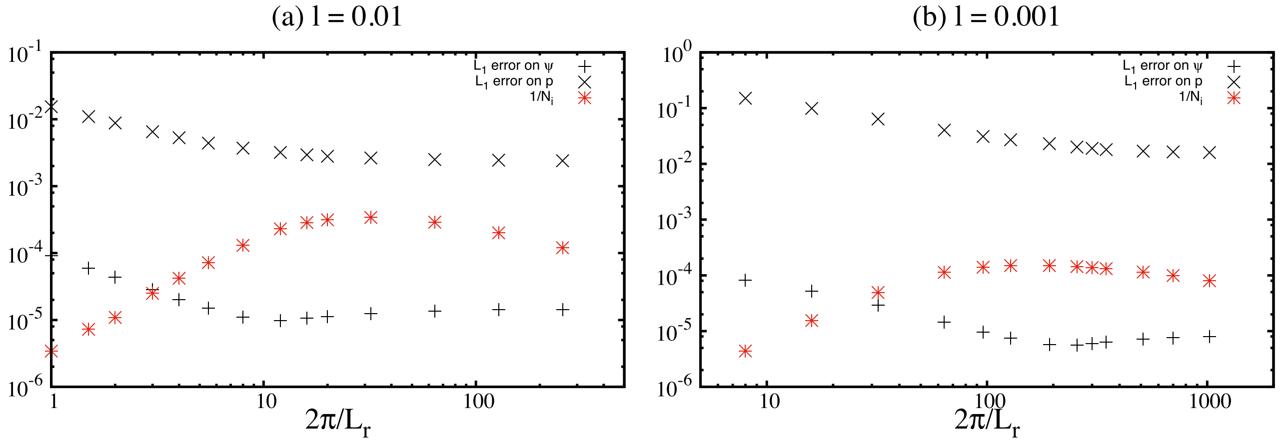

**Figure 2.** Error convergence for the 1D central layer problem. $L_1$ error on $\psi$ and $p$ variables, and inverse number of iterations $1/N_i$ as a function of $2\pi/L_\mathrm{r}$, for $l = 0.01$ (a) and $l = 0.001$ (b). The number of grid cells is 2000 and 8000 for $l = 0.01$ and 0.001, respectively. The steady state is obtained when the residual is reduced by a factor of $10^9$.

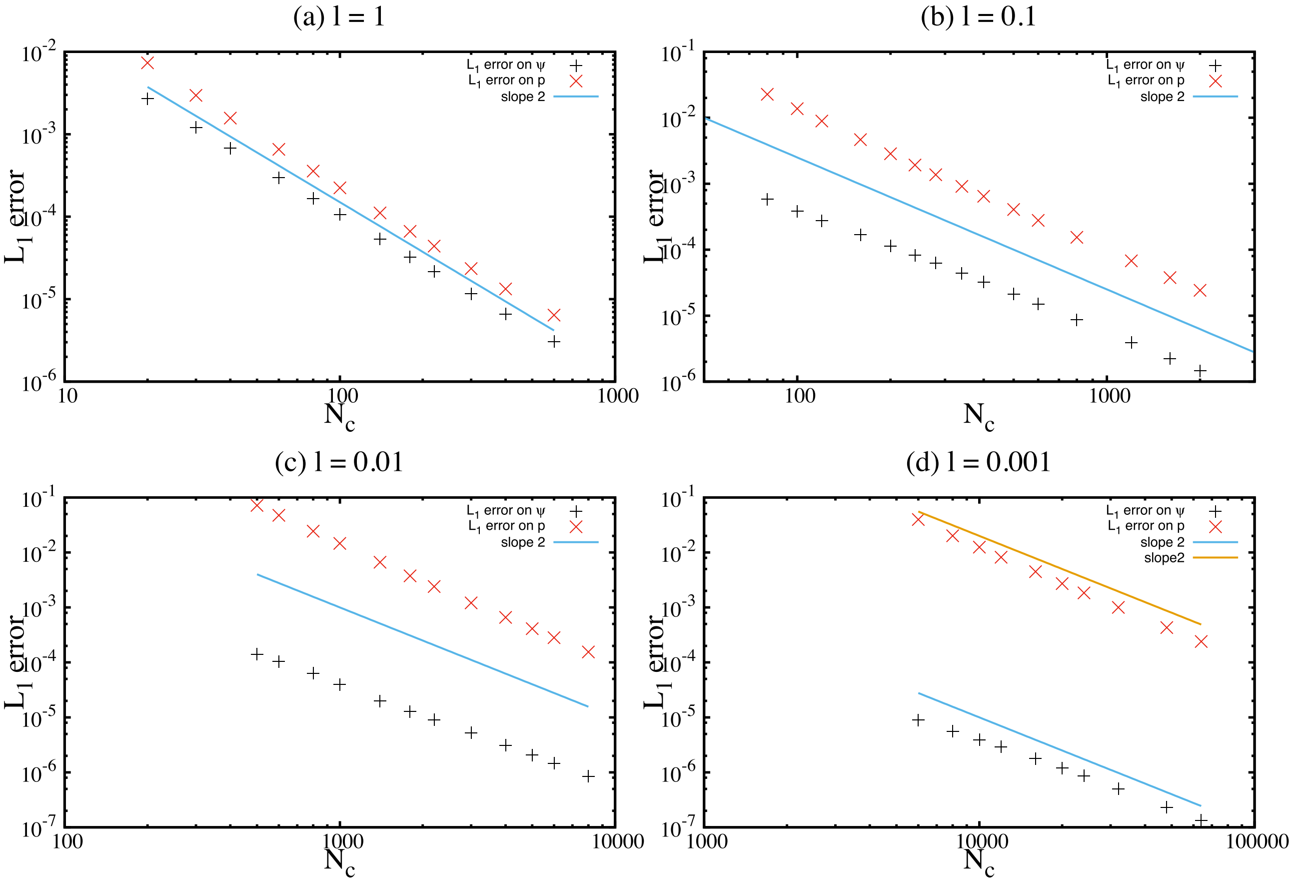

**Figure 3.** Error convergence for the 1D central layer problem. $L_1$ error on $\psi$ and $p$ variables as a function of the number of grid cells $N_\mathrm{c}$, for different $l$ values from $l = 1$ to 0.001. An optimal value of $L_\mathrm{r}^{-1} = 2\pi$ is chosen for $l = 1$ and 0.1, while it is $L_\mathrm{r}^{-1} = 16\pi$ and $L_\mathrm{r}^{-1} = 256\pi$ for $l = 0.01$ and 0.001, respectively. The second convergence order (slope 2) is also indicated with the plain line.

## 6 RESULTS ON MAGNETIC RECONNECTION PROCESS

### 6.1 Application to a magnetic annihilation solution

Magnetic annihilation solution is a particular magnetic reconnection process in which two antiparallel regions of magnetic field (directed along the $y$-directions) are swept together by the plasma flow and destroy one another (Priest & Sonnerup 1975). The solution is based on a stagnation-point flow,

$$\boldsymbol{V} = (-\alpha x, \alpha y), \tag{39}$$

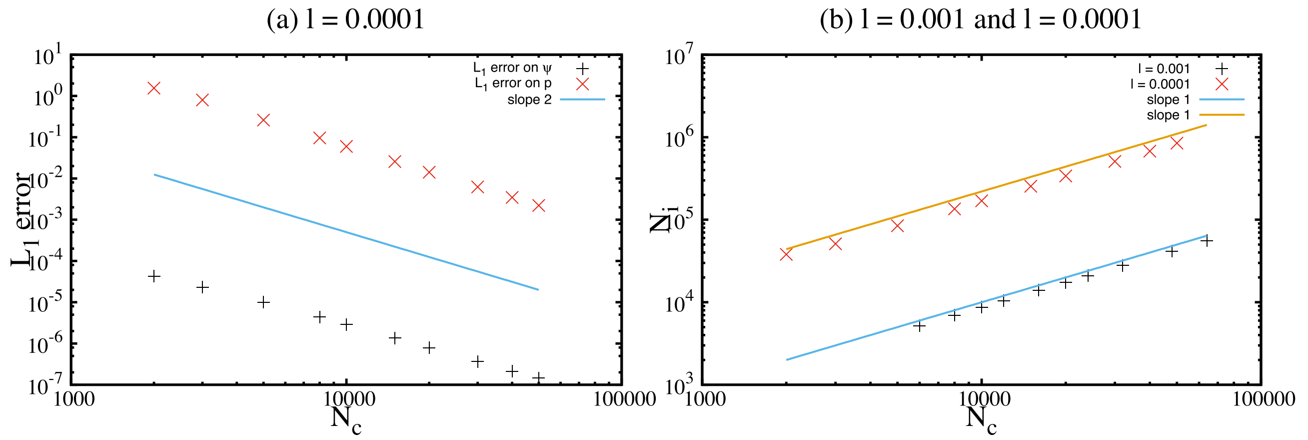
(a) l = 0.0001

(b) l = 0.001 and l = 0.0001

**Figure 4.** (a) Same as previous figure for $l = 0.0001$, where an optimal value of $L_r^{-1} = 2048\pi$ is chosen. A non-uniform grid is used. (b) The total number of iterations $N_i$ for final convergence as a function of the number of grid cells $N_c$, obtained for the two cases, $l = 0.001$ and 0.0001. The first convergence order (slope 1) is plotted in plain line.

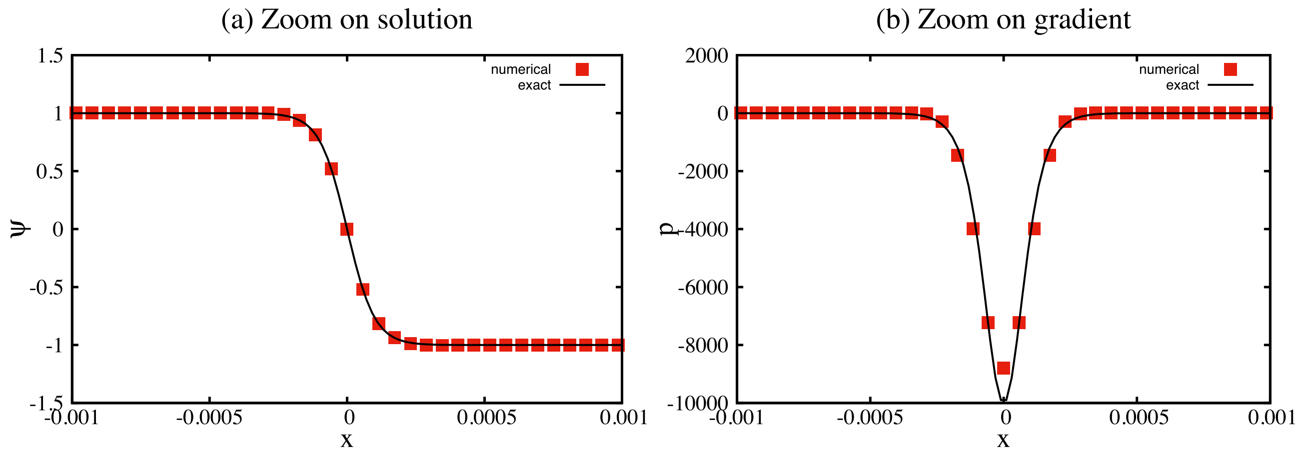
(a) Zoom on solution

(b) Zoom on gradient

**Figure 5.** Solution for 1D central layer problem. Zoom (on the central region at $x = 0$) for $\psi$ variable (a) and $p$ variable (b), for the $l = 0.0001$ case, employing 2000 non-uniformly distributed grid cells (lowest resolution in previous figure). The exact solution is also plotted in plain line for comparison.

where $\alpha$ is a positive real given constant. In the limit of vanishing viscosity (i.e. for $\nu = 0$), the exact steady state solution for the magnetic field is

$$\boldsymbol{B} = (0, B_y(x)), \tag{40}$$

with

$$B_y(x) = \frac{E_\mathrm{d}}{\eta\mu} Daw(\mu x), \tag{41}$$

where $E_\mathrm{d}$ is the magnitude of a uniform electric field perpendicular to the $(x, y)$ plane, $\mu^2 = \alpha/(2\eta)$, and $Daw(x)$ is the Dawson function given by

$$Daw(x) = \int_0^x \exp(t^2 - x^2)\mathrm{d}t. \tag{42}$$

The role of $E_\mathrm{d}$ is to control the rate of energy conversion. This solution is the mutual annihilation of two equal and opposite antiparallel fields. In the limit of small resistivity, the solution exhibits a strong current sheet centred over the stagnation-point flow. The sheet has a thickness in the $x$-direction proportional to $\eta^{1/2}$, and can extend to infinity in the $y$-direction.

We have carried out computations to find the steady state solution for $\alpha = 1$ and $E_\mathrm{d} = 0.1$, in a square spatial domain $(x, y) \in [-L, L] \times [-L, L]$. We set $L = 1$ to define our normalization. Consequently, the global and local magnetic Reynolds numbers can be written as $R_\mathrm{m} = L\alpha/\eta = 1/\eta$ and $R_\mathrm{m}^* = LV/\eta = V/\eta$ in our units, respectively.

These values are the typical one used in the magnetic reconnection literature research (Watson & Craig 1998), and are not varied here. As a non-viscous solution is required for this problem, a zero viscosity coefficient $\nu = 0$ is employed in our scheme. Consequently, equations (25) and (26) are not implemented and the associated gradient variables of $\Omega$ not used. Different resistivity parameter values are considered for $\eta$, as it represents the key parameter for the solution. In a way similar to the 1D test case, the convergence is considered to be obtained when the initial residual of the system is reduced by seven orders of magnitude in the $L_1$ norm. The residual is now taken to be the maximum residual component over the 12 variables. The CFL number is taken to be 0.99 in all cases. As for the previous 1D example, an initial guess must be provided for the variables that are initialized with zero values in the interior of the domain. At the boundaries, the exact Dirichlet conditions are imposed in a weak form on five variables, namely the magnetic field components ($p_\psi$, and $q_\psi$ in our variables), the velocity components, and the vorticity. The boundary values on the other variables are in fact computed with our numerical scheme.

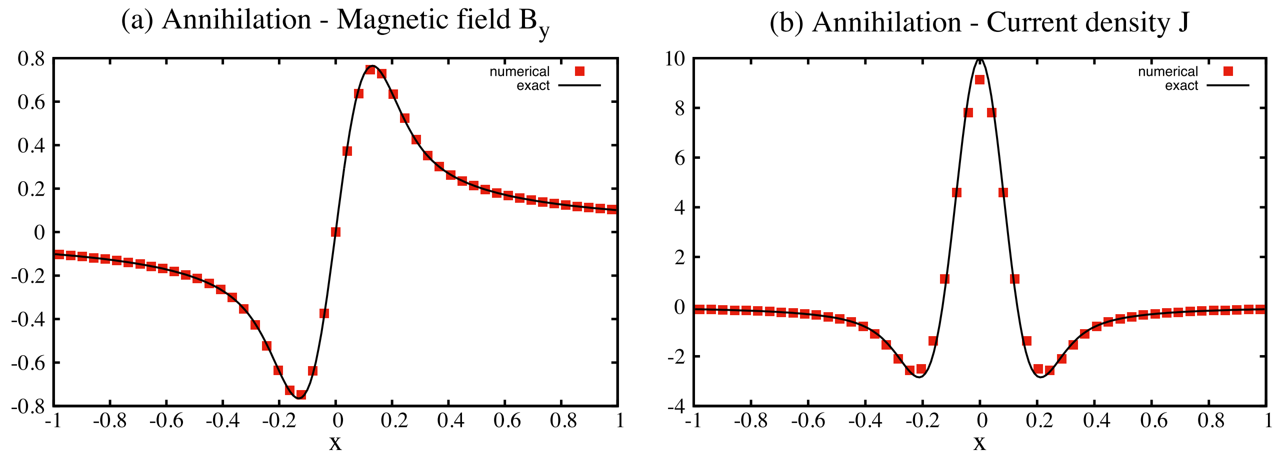

**Figure 6.** Magnetic annihilation solution (cut at $y = 0$) obtained for $p_\psi = B_y(x)$ and $J(x)$ using a low spatial resolution of 50 × 50 grid cells, for a case with $\eta = 0.01$ ($R_\mathrm{m} = 10^2$). The exact solutions is plotted using plain line for comparison.

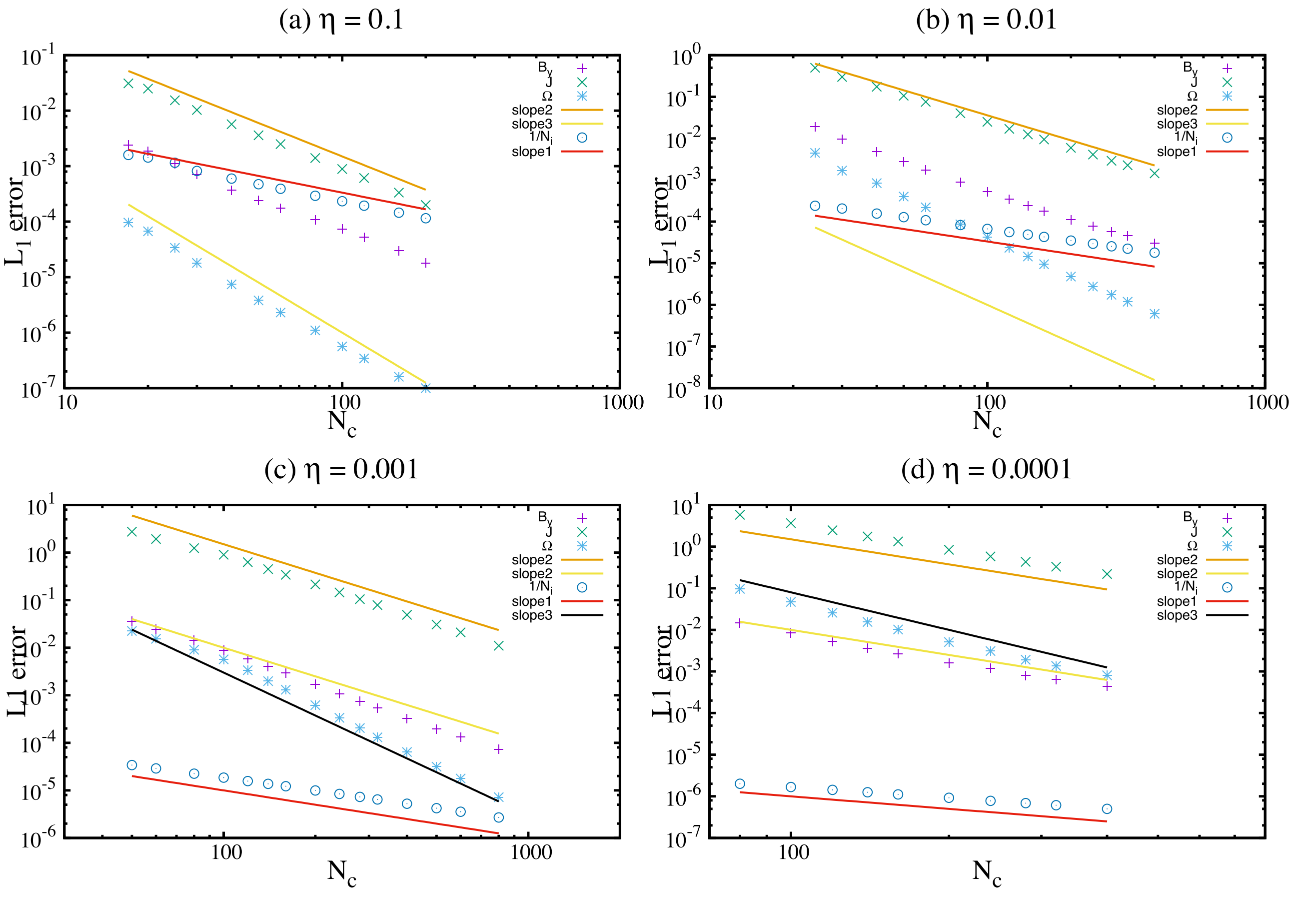

**Figure 7.** Error convergence for the magnetic annihilation problem. $L_1$ error on $B_y$, $J$, and $\Omega$, as a function of the number of grid cells $N_\mathrm{c}$ in each direction. The inverse number of iterations $1/N_i$ necessary to reduce the initial residual by seven orders of magnitude is also plotted. The linear (slope 1), parabolic (slope 2), and cubic (slope 3) convergence orders are also indicated with plain line. Optimal $2\pi/L_\mathrm{r}$ values of 2, 4, 10, and 36 are used for $\eta = 0.1$ (a), $\eta = 0.01$ (b), $\eta = 0.001$ (c), and $\eta = 0.0001$ (d), respectively. A non-uniform cell spacing in $x$-direction is used for $\eta = 0.0001$ (d).

The typical numerical solution [$B_y(x)$ and $J(x)$ variation at $y = 0$] can be seen in Fig. 6, for a case with $\eta = 0.01$ ($R_\mathrm{m} = 10^2$). At this relatively low resolution of 50 × 50 grid cells, the expected analytical solution is already well approximated. Secondly, we examined the spatial order of accuracy of the scheme. As explained in the previous section, depending on runs, optimal values of the $L_\mathrm{r}$ parameter have been carefully selected for optimal convergence.

The $L_1$ error convergence results measured on $B_y$, $J$, and $\Omega$ are plotted for four different $\eta$ values ranging between 0.1 and 0.0001. The corresponding range of magnetic Reynolds numbers explored is thus $R_\mathrm{m} \in [10 : 10^4]$. The errors on other variables lead to a similar dependence and are consequently not shown. The second-order accuracy is clearly obtained for $B_y$, and $J$, independently of $\eta$. The results are even better for $\Omega$ (close to third order), probably due to

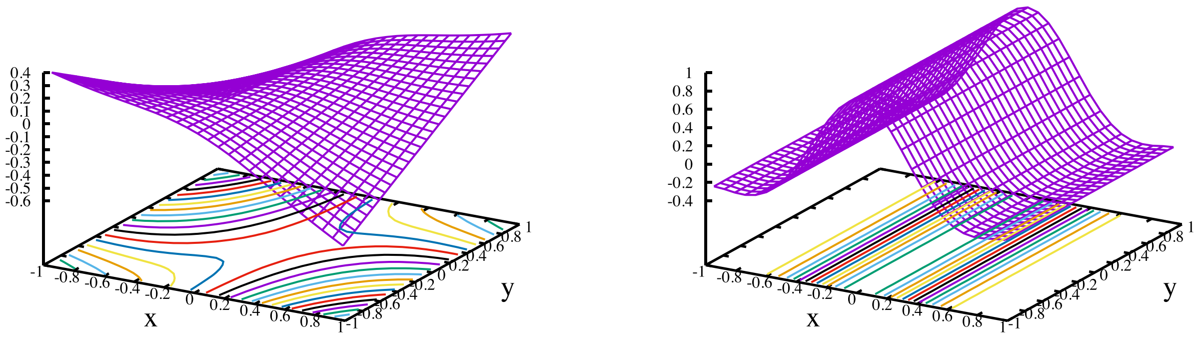

(a) ψ and magnetic field lines

(b) Current density J

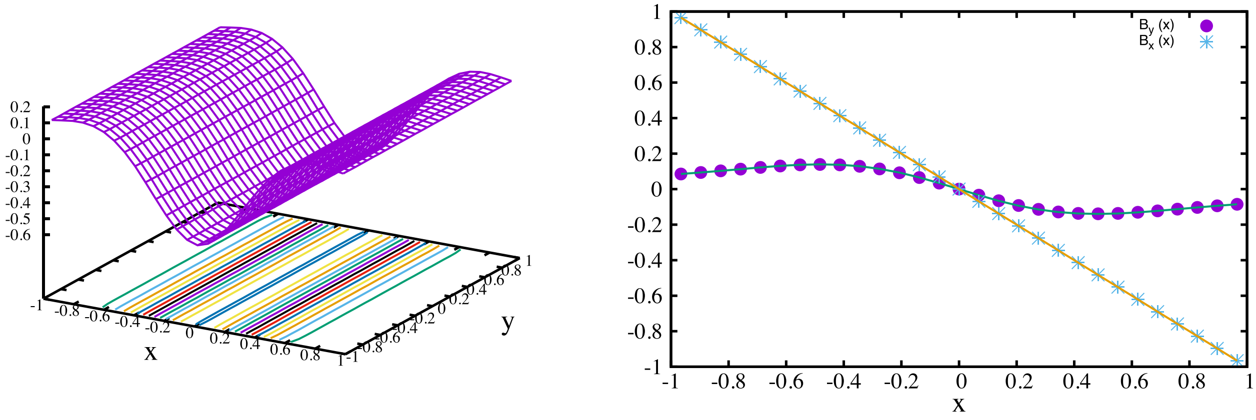

(c) vorticity Ω

(d) velocity $V_x$ and $V_y$

**Figure 8.** Reconnective diffusion solution obtained for $\eta = 0.1$ and $\beta = 0.5$ using a spatial resolution of $30 \times 30$ grid cells. The flux variable $\psi(x, y)$ and isocontours (in bottom plane) representing the magnetic field lines, the current density $J(x, y)$, the vorticity variable $\Omega(x, y)$, and velocity components ($V_x(x)$, $V_y(x)$) at $y = 0$ are plotted in the different panels (a),(b),(c),(d), respectively.

the particular zero vorticity solution expected for this problem. The number of iterations necessary for final convergence is also shown to scale linearly with the number of grid cells, as expected from our CFL criterion. Finally, one must note that our scheme keeps the same convergence properties even when a non-uniform grid is used, as can be seen in Fig. 7 (panel d) for the less dissipative case with $R_{\rm m} = 10^4$. The grid is stretched only in the $x$-direction, as required by the expected $x$-gradient solution which scales as $R_{\rm m}^{-1/2}$.

### 6.2 Application to a reconnective diffusion solution

As an natural extension of the previous reconnection model, the solution of the called reconnective diffusion solution has been obtained by Craig & Henton (1995). It corresponds to the velocity and magnetic field profiles of the form:

$$\boldsymbol{V} = (-\alpha x, \alpha y - \frac{\beta}{\alpha}\frac{E_{\rm d}}{\eta\mu} Daw(\mu x)), \quad (43)$$

and

$$\boldsymbol{B} = (\beta x, -\beta y + \frac{E_{\rm d}}{\eta\mu} Daw(\mu x)), \quad (44)$$

respectively. The new definition of $\mu$ parameter is now

$$\mu^2 = \frac{\alpha^2 - \beta^2}{2\eta\alpha}, \quad (45)$$

where a new positive real parameter $\beta < \alpha$ is introduced. Note that the annihilation solution is naturally recovered when $\beta = 0$. The reconnective diffusion exhibits diffusion across one separatrix like the diffusive annihilation solution, but the dominant process across the other separatrix is advection like a classical reconnection picture. As a shear flow exists across a global current layer, there is a symmetry breaking compared to the annihilation process (Watson, Priest & Craig 1998).

Using the same procedure described in the previous section, we have carried out computations to find steady state solution for $\alpha = 1$, $E_{\rm d} = 0.1$, and different resistivity values for $\eta$. We have also explored different $\beta$ values, as $\beta$ determines the departure of the 2D magnetic field reconnective solution from the previous purely 1D annihilation reconnection solution. The typical numerical solution obtained can be seen in Fig. 8, for $\beta = 0.5$ and $\eta = 0.1$ ($R_{\rm m} = 10$), for a low-resolution case of $30 \times 30$ grid cells. The latter figure clearly illustrates the 2D character of $\psi$ and corresponding magnetic field lines compared to the annihilation solution. The contours of $\psi$ also exhibits the magnetic reconnection process as they represent the magnetic field lines. Indeed, Fig. 8 (left a-panel) displays the different regions, with a group of field lines advected towards the central region and another group of outflowing reconnected field lines. Secondly, we examined the spatial order of accuracy of the scheme. The $L_1$ errors on different chosen variables are plotted in Fig. 9 for different $\eta$ values (ranging between 0.03 and 0.0003 in the different panels), using a given $\beta = 0.25$. The corresponding

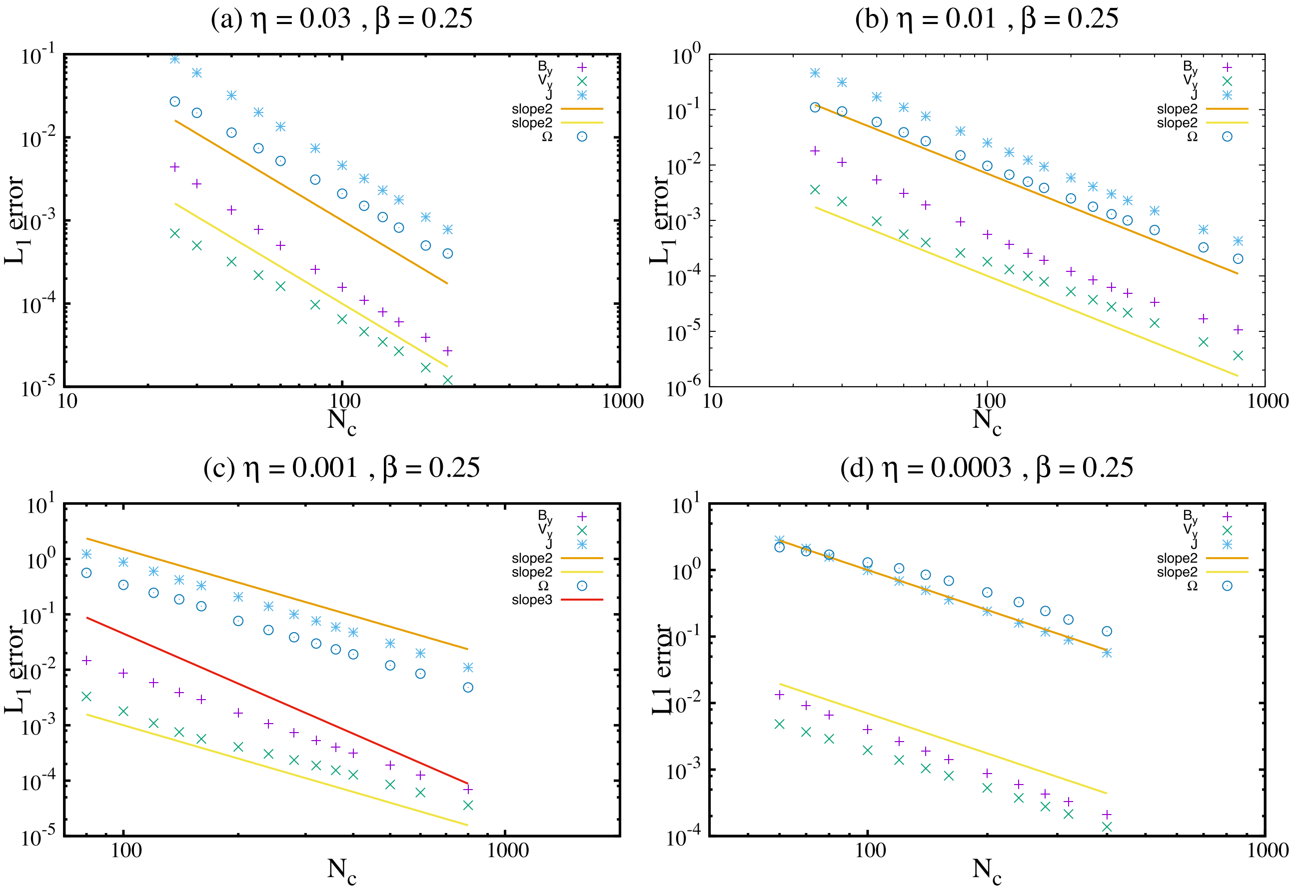

**Figure 9.** Error convergence for the reconnective diffusion problem. $L_1$ error on $B_y$, $V_y$, $J$, and $\Omega$, as a function of the number of grid cells $N_c$ in each direction. The linear (slope 1), parabolic (slope 2), and cubic (slope 3) convergence orders are also indicated with plain line. Optimal $2\pi/L_r$ values of 2, 3, 10, and 30 are used for $\eta = 0.03$ (a), $\eta = 0.01$ (b), $\eta = 0.001$ (c), and $\eta = 0.0003$ (d), respectively. A non-uniform cell spacing in $x$-direction is used for $\eta = 0.0003$ case.

range of magnetic Reynolds numbers explored is thus $R_m \in [33 : 3.3 \times 10^3]$. A convergence order close to two is obtained for all the variables for all the different $\eta$ values. Note again, that the result also hold when a non-uniform grid is employed, as it is the case for the lowest resistive case (panel d).

Let us note the remarkable result obtained for the evaluation of the $J$ variable, which also exhibits a convergence very close to the second order. Indeed, as the current density is obtained as a second-order spatial derivative of the main variable $\psi$, $J$ is evaluated with a lower order of accuracy compared to the main variables in traditional schemes. This is important because the reconnection mechanism requires a careful treatment of the $\eta J$ term which determines the solution. This is illustrated in Fig. 10, where is plotted the $L_1$ error on $J$ for different $\beta$ values. Finally, we have checked that the number of iterations needed for convergence also scales with the number of grid cells.

## 7 DISCUSSION AND CONCLUSION

In this work, we have extended the hyperbolic method initially derived for the diffusion equation (Nishikawa 2007) to a 2D set of incompressible dissipative MHD equations. This completes the application to advection-diffusion and Navier–Stokes systems. The hyperbolic formulation of the resistive and viscous terms allowed us to construct a simple finite-volume scheme discretization on a rectangular grid, using an approximate Riemann solver to handle the dissipative and advective flux in the same way. For the sake of clarity, a simple second-order upwind flux formulation is chosen in this work.

It is shown that our hyperbolic scheme is able to produce stationary solutions for two non-viscous reconnection problems, namely the magnetic annihilation and reconnective diffusion for which exact analytical expressions exist (Watson et al. 1998). The first advantage of this approach over traditional schemes is demonstrated through its consistent accuracy over a wide range of magnetic Reynolds numbers. Indeed, the spatial second order of convergence is closely obtained for the main and gradient variables as well. Secondly, the convergence towards the steady state scales only linearly with the cell width $h$, giving thus a $O(1/h)$ acceleration over conventional schemes. Our hyperbolic method has a clear analogy with the hyperbolic divergence cleaning technique used in MHD codes to handle the divergence-free condition of the magnetic field (Dedner et al. 2002). Indeed, an additional numerical scalar variable is introduced in order to advect and diffuse the divergence errors to the domain boundaries. A corresponding scalar equation is also added and coupled to the magnetic field induction equation, leading thus to an hyperbolic system. As a major difference, this latter hyperbolic technique is introduced to handle a numerical term and not a physical dissipation term. It is also implemented in the true time evolution of the system contrary to our pseudo-time implementation.

The next step in the development of the hyperbolic method for MHD is the extension to time-dependent solutions. Accurate

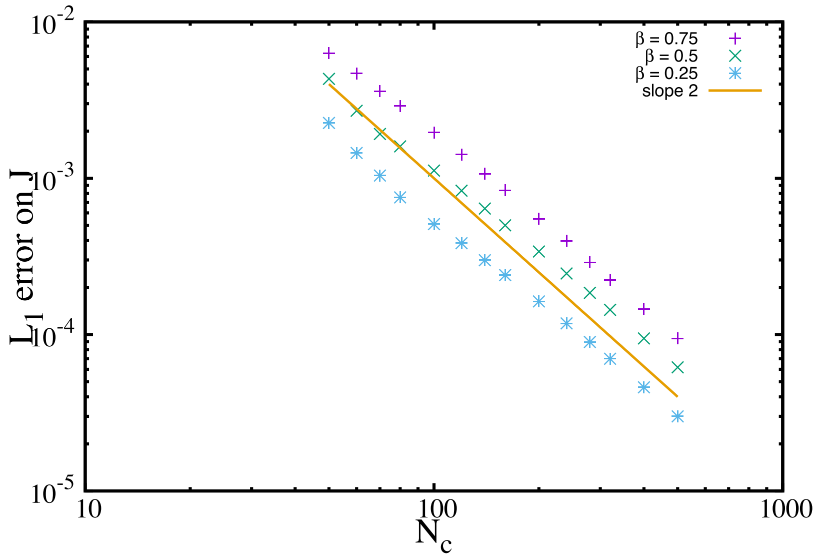

**Figure 10.** Error convergence for the reconnective diffusion problem. $L_1$ error on $J$ as a function of the number of grid cells $N_c$ in each direction, for different $\beta$ values. A resistivity value of $\eta = 0.003$ is employed for all cases. The parabolic (slope 2) convergence order is also indicated with plain line.

time-dependent computations are possible by using implicit time integration. Indeed, efficient high-order hyperbolic schemes have been proposed for the advection-diffusion equation, with the idea to converge to successive pseudo-steady states that are solutions at successive physical time steps of the time-dependent equations (Mazaheri & Nishikawa 2014). In order to speed up the convergence procedure iteration at each time step, the scheme presented in this work would probably require some improvements like higher order spatial reconstruction and/or an implicit pseudo-time solver (Nakashima, Watanabe & Nishikawa 2016). Such time-dependent solutions also require some spatial or/and temporal dependences of the resistivity profile, which are essential in studies related to solar flares. We have checked that our scheme also works when a spatially localized profile is prescribed on the 1D model equation. The extension to the MHD model is actually under development.

Many aspects are considered to be fairly well understood for 2D MHD reconnection. This is however not the case of the plasmoid induced reconnection regime (Samtaney et al. 2009; Baty 2012; Loureiro et al. 2012), which is characterized by a complicated time-dependent bursty dynamics (Loureiro et al. 2009). There is actually a great deal of interest on the subject, as the associated reconnection is considered to give an efficient energy mechanism on a fast time-scale that is nearly independent of the resistivity. This is of considerable importance to explain solar flares. The numerical investigation of the role of plasmoids in magnetic reconnection is complicated, as conventional codes lack some convergence properties due to the stochastic feature of the associated reconnection mechanism (Keppens et al. 2013). Moreover, the plasmoid regime is also reached for sufficiently high Reynolds number. The use of our hyperbolic scheme would be thus particularly promising in this context.

## ACKNOWLEDGEMENTS

The authors thank P. Helluy, J. Petri, and P. Ackerer for fruitful discussions. HB acknowledges support by French National Research Agency (ANR) through Grant ANR-13-JS05-0003-01 (Project EMPERE). We also acknowledge computational facilities available at Equip@Meso of the Université de Strasbourg. We sincerely thank the anonymous referee for useful suggestions that helped improve the content of the paper.

## REFERENCES

Baty H., 2012, Phys. Plasmas, 19, 092110
Baty H., Forbes T. G., Priest E. R., 2014, Phys. Plasmas, 21, 112111
Craig I. J. D., Henton S. M., 1995, ApJ, 450, 280
Dedner A., Kemm F., Kröner D., Munz C.-D., Schnitzer T., Wesenberg M., 2002, J. Comput. Phys., 175, 645
Gassner G., Lörcher F., Munz C.-D., 2007, J. Comput. Phys., 224, 1049
Keppens R., Porth O., Galsgaard K., Frederiksen J. T., Restante A. L., Lapenta G., Parnell C., 2013, Phys. Plasmas, 20, 092109
Loureiro N. F., Uzdensky D. A., Schekochihin A. A., Cowley S. C., Yousef T. A., 2009, MNRAS, 399, L146
Loureiro N. F., Samtaney R., Schekochihin A. A., Uzdensky D. A., 2012, Phys. Plasmas, 19, 042303
Lowrie R. B., Morel J. E., 2002, Int. J. Numer. Methods Fluids, 40, 413
Mazaheri A., Nishikawa H., 2014, Comput. Fluids, 102, 131
Nakashima Y., Watanabe N., Nishikawa H., 2016, Proc. of 54th AIAA Aerospace Sciences Meeting, AIAA Paper 2016-1001, San Diego, CA
Nishikawa H., 2007, J. Comput. Phys., 227, 315
Nishikawa H., 2010, J. Comput. Phys., 227, 3989
Nishikawa H., 2011, Proc. of 20th AIAA Computational Fluid Dynamics Conference, AIAA Paper 2011-3044, Honolulu, Hawaii
Nishikawa H., 2012, J. Comput. Phys., 231, 6393
Nishikawa H., 2014, J. Comput. Phys., 256, 791
Nishikawa H., Roe P. L., 2004, Computational Fluid Dynamics. Springer-Verlag, Berlin, p. 799
Orszag S. A., Tang C. M., 1979, J. Fluid Mech., 90, 129
Porth O., Xia C., Hendrix T., Moschou S. P., Keppens R., 2014, ApJS, 214, 4
Priest E. R., Forbes T. G., 2000, Magnetic Reconnection. Cambridge Univ. Press, Cambridge
Priest E. R., Sonnerup B. U. Oe., 1975, Geophys. J., 41, 405
Samtaney R., Loureiro N. F., Uzdensky D. A., Schekochihin A. A., Cowley S. C., 2009, Phys. Rev. Lett., 103, 105004
Watson P. G., Craig I. J. D., 1998, ApJ, 505, 363
Watson P. G., Priest E. R., Craig I. J. D., 1998, Geophys. Astrophys. Fluid Dyn.. 88, 165
Younes A., Ackerer P., Chavent G., 2004, Int. J. Numer. Methods Eng., 59, 365

## APPENDIX A

### A1 Discretization of the MHD hyperbolic method

The general form is

$$\frac{\partial \boldsymbol{U}}{\partial \tau} + \frac{\partial F}{\partial x} + \frac{\partial \boldsymbol{G}}{\partial y} = \boldsymbol{S}, \tag{A1}$$

leading to

$$\boldsymbol{U} = \begin{pmatrix} \psi \\ p_\psi \\ q_\psi \\ \Omega \\ p_\Omega \\ q_\Omega \\ V_x \\ p_x \\ q_x \\ V_y \\ p_y \\ q_y \end{pmatrix}, \boldsymbol{F} = \begin{pmatrix} V_x\psi - \eta p_\psi \\ -\psi/T_\psi \\ 0 \\ V_x\Omega - \nu p_\Omega + f \\ -\Omega/T_\Omega \\ 0 \\ -p_x \\ -V_x/T_\mathrm{r} \\ 0 \\ -p_y \\ -V_y/T_\mathrm{r} \\ 0 \end{pmatrix}, \boldsymbol{G} = \begin{pmatrix} V_y\psi - \eta q_\psi \\ 0 \\ -\psi/T_\psi \\ V_y\Omega - \nu q_\Omega + g \\ 0 \\ -\Omega/T_\Omega \\ -q_x \\ 0 \\ -V_x/T_\mathrm{r} \\ -q_y \\ 0 \\ -V_y/T_\mathrm{r} \end{pmatrix}, \boldsymbol{S} = \begin{pmatrix} E_\psi \\ -p_\psi/T_\psi \\ -q_\psi/T_\psi \\ E_\Omega \\ -p_\Omega/T_\Omega \\ -q_\Omega/T_\Omega \\ q_\Omega \\ -p_x/T_\mathrm{r} \\ -q_x/T_\mathrm{r} \\ -p_\Omega \\ -p_y/T_\mathrm{r} \\ -q_y/T_\mathrm{r} \end{pmatrix}.$$

Note that the $-\nabla.(J\boldsymbol{B})$ term is integrated in the flux via $f = -Jq_\psi$ and $g = Jp_\psi$.

### A2 Numerical fluxes at cell interfaces

The fluxes for the $\psi$-equation are

$$\frac{1}{2}[(V_n\psi)_\mathrm{R} + (V_n\psi)_\mathrm{L}] - \frac{1}{2}|V_n|(\psi_\mathrm{R} - \psi_\mathrm{L}), \tag{A2}$$

and,

$$\frac{1}{2}[(-\eta g_\psi)_\mathrm{R} + (-\eta g_\psi)_\mathrm{L}] - \frac{1}{2}\sqrt{\eta/T_\psi}(\psi_\mathrm{R} - \psi_\mathrm{L}), \tag{A3}$$

for the advective and resistive part, respectively. We use $V_n = V_x$ and $V_n = V_y$ for the $x$ and $y$ contributing advective flux, respectively. We also have $g_\psi = p_\psi$ and $g_\psi = q_\psi$ for the $x$ and $y$ contributing resistive flux, respectively.

The fluxes for the $p_\psi$ and $q_\psi$ equations are, respectively,

$$\frac{1}{2}[(-\psi/T_\psi)_\mathrm{R} + (-\psi/T_\psi)_\mathrm{L}] - \frac{1}{2}\sqrt{\eta/T_\psi}[(p_\psi)_\mathrm{R} - (p_\psi)_\mathrm{L}], \tag{A4}$$

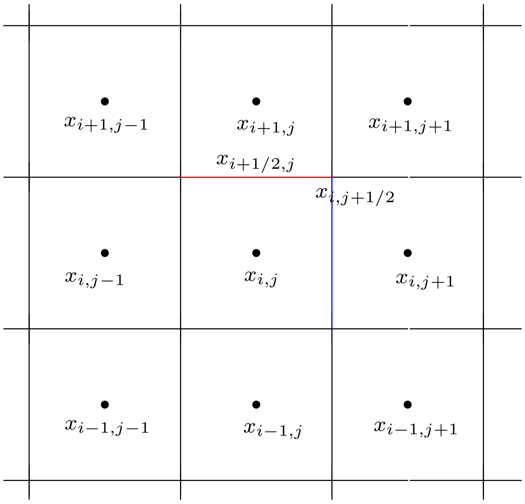

**Figure A1.** Space discretization in 2D.

and,

$$\frac{1}{2}[(-\psi/T_{\psi})_{\rm R}+(-\psi/T_{\psi})_{\rm L}]-\frac{1}{2}\sqrt{\eta/T_{\psi}}[(q_{\psi})_{\rm R}-(q_{\psi})_{\rm L}]. \tag{A5}$$

The fluxes for the $\Omega$-equation are

$$\frac{1}{2}[(V_n\Omega)_{\rm R}+(V_n\Omega)_{\rm L}-\frac{1}{2}\,|V_n|\,(\Omega_{\rm R}-\Omega_{\rm L}) \tag{A6}$$

and

$$\frac{1}{2}[(-\nu g_{\Omega})_{\rm R}+(-\nu g_{\Omega})_{\rm L}]-\frac{1}{2}\sqrt{\nu/T_{\Omega}}(\Omega_{\rm R}-\Omega_{\rm L}) \tag{A7}$$

for the advective and viscous part, respectively, with $g_{\Omega}=p_{\Omega}$ and $g_{\Omega}=q_{\Omega}$ for the $x$ and $y$ contributing viscous flux, respectively.

The fluxes for $p_{\Omega}$ and $q_{\Omega}$ equations are, respectively,

$$\frac{1}{2}[(-\Omega/T_{\Omega})_{\rm R}+(-\Omega/T_{\Omega})_{\rm L}-\frac{1}{2}\sqrt{\nu/T_{\Omega}}[(p_{\Omega})_{\rm R}-(p_{\Omega})_{\rm L}] \tag{A8}$$

and

$$\frac{1}{2}[(-\Omega/T_{\Omega})_{\rm R}+(-\Omega/T_{\Omega})_{\rm L}-\frac{1}{2}\sqrt{\nu/T_{\Omega}}[(q_{\Omega})_{\rm R}-(q_{\Omega})_{\rm L}]. \tag{A9}$$

The fluxes corresponding to the $-\nabla.(J\boldsymbol{B})$ specific term ($f$ and $g$ terms in equation A1) is evaluated by using

$$-\frac{1}{2}[(Jq_{\psi})_{\rm L}+(Jq_{\psi})_{\rm R}] \tag{A10}$$

and

$$-\frac{1}{2}[(Jp_{\psi})_{\rm L}+(Jp_{\psi})_{\rm R}] \tag{A11}$$

for the $x$ and $y$ directed flux, respectively. Note that $J$ is computed using $J=-\frac{\partial p_{\psi}}{\partial x}-\frac{\partial q_{\psi}}{\partial y}$.

The fluxes for the $V_x$ and associated derivatives $p_x$ and $q_x$ equations are, respectively,

$$\frac{1}{2}[(-g_x)_{\rm R}+(-g_x)_{\rm L}]-\frac{1}{2}\sqrt{1/T_{\rm r}}[(V_x)_{\rm R}-(V_x)_{\rm L}], \tag{A12}$$

$$\frac{1}{2}[(-V_x/T_{\rm r})_{\rm R}+(-V_x/T_{\rm r})_{\rm L}]-\frac{1}{2}\sqrt{1/T_{\rm r}}[(p_x)_{\rm R}-(p_x)_{\rm L}], \tag{A13}$$

$$\frac{1}{2}[(-V_x/T_{\rm r})_{\rm R}+(-V_x/T_{\rm r})_{\rm L}]-\frac{1}{2}\sqrt{1/T_{\rm r}}[(q_x)_{\rm R}-(q_x)_{\rm L}]. \tag{A14}$$

We use the definition $g_x=p_x$ and $g_x=q_x$ for the $x$ and $y$ contributing flux, respectively.

The fluxes for the $V_y$ and associated derivatives $p_y$ and $q_y$ equations are, respectively,

$$\frac{1}{2}[(-g_y)_{\rm R}+(-g_y)_{\rm L}]-\frac{1}{2}\sqrt{1/T_{\rm r}}[(V_y)_{\rm R}-(V_y)_{\rm L}], \tag{A15}$$

$$\frac{1}{2}[(-V_y/T_{\rm r})_{\rm R}+(-V_y/T_{\rm r})_{\rm L}]-\frac{1}{2}\sqrt{1/T_{\rm r}}[(p_y)_{\rm R}-(p_y)_{\rm L}], \tag{A16}$$

$$\frac{1}{2}[(-V_yT_{\rm r})_{\rm R}+(-V_y/T_{\rm r})_{\rm L}]-\frac{1}{2}\sqrt{1/T_{\rm r}}[(q_y)_{\rm R}-(q_y)_{\rm L}]. \tag{A17}$$

We use the definition $g_y=p_y$ and $g_y=q_y$ for the $x$ and $y$ contributing flux, respectively.

### A3 Source term evaluation

The source term is evaluated using the point integration scheme:

$$\int_{I_{i,j}} \boldsymbol{S}_{i,j}\mathrm{d}x\mathrm{d}y \approx \boldsymbol{S}_{i,j} h_x h_y = h_x h_y \begin{pmatrix} E_{\psi_{i,j}} \\ -p_{\psi_{i,j}}/T_\psi \\ -q_{\psi_{i,j}}/T_\psi \\ E_{\Omega_{i,j}} \\ -p_{\Omega_{i,j}}/T_\Omega \\ -p_{\Omega_{i,j}}/T_\Omega \\ q_{\Omega_{i,j}} \\ -p_{x_{i,j}}/T_\mathrm{r} \\ -q_{x_{i,j}}/T_\mathrm{r} \\ -p_{\Omega_{i,j}} \\ -p_{y_{i,j}}/T_\mathrm{r} \\ -q_{y_{i,j}}/T_\mathrm{r} \end{pmatrix}. \tag{A18}$$

### A4 CFL criterion

The 2D pseudo-time marching implementation obeys now a CFL limit,

$$\Delta\tau = \mathrm{CFL} \times \mathrm{Min}\left[\frac{h_x h_y}{h_y(\sqrt{1/T_\mathrm{r}} + \sqrt{\eta/T_\psi} + \sqrt{\nu/T_\Omega} + a_x) + h_x(\sqrt{1/T_\mathrm{r}} + \sqrt{\eta/T_\psi} + \sqrt{\nu/T_\Omega} + a_y)}\right], \tag{A19}$$

where $a_x = |V_x|$ and $a_y = |V_y|$. As in most of our applications, we are interested in applications where we have the ordering $\nu < <\eta < <1$, the previous CFL criterion can reduce to (in first approximation)

$$\Delta\tau = \mathrm{CFL} \times \mathrm{Min}\left[\frac{h_x h_y}{h_y(\sqrt{1/T_\mathrm{r}} + a_x) + h_x(\sqrt{1/T_\mathrm{r}} + a_y)}\right]. \tag{A20}$$

This paper has been typeset from a TEX/LATEX file prepared by the author.